VIII International Conference on Particle-Based Methods
PARTICLES 2023
U. Perego, M. Cremonesi, A. Franci (Eds)

How the Packing Density and Penetration Resistance is Influenced by Particle Shape: DEM Modelling of Plate Penetration in Granular Media

G.J. van Selm*, M.J. Mohajeri, H. Shi and D.L. Schott

Department of Maritime and Transport Technology
Faculty of Mechanical Engineering
Delft University of Technology
2628CD Delft, The Netherlands

Abstract. Granular materials play a crucial role in various geotechnical, mining, and bulk-handling applications. Understanding their mechanical properties is essential for optimal use in these industries. Traditional experimental methods like Cone Penetration Test (CPT) and open pile testing have limitations on their repeatability and offer little insight into the contact mechanics. The Discrete Element Method (DEM) is a powerful tool for investigating and simulating granular material behaviour at the element scale and provides deeper understanding in geometry-material interactions. However, due to computational costs, spherical particles are often preferred, though they may not always capture realistic particle interactions.

In the current study, the packing density and the penetration resistance of particle beds with different particle shapes, including sphere, multi-spheres and polyhedrons, are compared using a plate penetration test modelled in DEM. Sensitivity analyses are performed for sliding friction, consolidation pressure, and Particle Size Distribution (PSD). Results indicate that polyhedral shapes show lower penetration resistance compared to spherical and multi-spherical shapes. Sliding friction has the most significant impact on resistance, while consolidation pressure has minimal effect on porosity. The study highlights the importance of particle shape in granular media modelling and emphasizes the need for further research in this area.

Keywords: DEM, Granular Materials, Particle Shape, Penetration Test, Packing

1 INTRODUCTION

Granular coarse materials such as gravel, grains and minerals are common in geotechnical, mining and bulk handling applications. Therefore, thorough understanding of their mechanical properties is required for optimal application of these granular materials [1]. Several research methods have investigated the penetration resistance of coarse materials, by using the Cone Penetration Test (CPT) [2] [3] , plate penetration [4] or open pile testing [5]. However, these tests have important limitations, especially for coarser materials, where the ratio of median particle diameter over the width of the penetration tool (d_{50}/w) is close to or larger than 1. They are difficult to control precisely, which severely impacts repeatability of experiments. Additionally, the mechanics between a geometry and the granular material are poorly understood, which forces interpretation by empirical approaches [6].

The Discrete Element Method (DEM) is widely used to investigate the behaviour of granular material at element scale, as it offers accessible information at each particle-particle interaction.

Recently, DEM has proven to be suitable for the modelling of penetration as well, such as cone penetration resistance or large pile jacking [7]. Granular materials are mostly found with non-spherical shapes, and these show a different material behaviour compared to (near) spherical particles, such as glass beads and iron pellets. Modelling coarse material has been done successfully, by implementing a spherical shape to reduce computational costs. To compensate for the shape effect, the rolling friction coefficient has been calibrated as well [8]. However, using spheres creates limitations in capturing the geometrical effect, such as interlocking between particles and particle packing. It is thus preferable to model the particles using more realistic, non-spherical shapes, like clumps or polyhedrons [9]. With the development of computer technology and higher requirements of computational accuracy, the influence of particle shape on the mechanical properties of granular material has become a main concern of DEM [10]. However, unlike spherical particles, the number of published works on non-spherical particle behaviour is still very limited [11], and it is not yet clear how the strength of a particle bed composed of angular polyhedral particles, compares to a particle bed with spherical particles.

The aim of this work is to compare the packing density and resistance of particle beds with different particle shapes, including sphere, multi-spheres and polyhedron. A DEM plate penetration test is designed, which is representative for various applications, such as pile driving and grabbing processes. For each particle shape a sensitivity analysis is performed concerning the sliding friction between particles, consolidation pressure and Particle Size Distribution (PSD).

2 MODELLING METHODS

In this research the Altair EDEM (version 2022.2) software package is used. This is a suitable solution to simulate both spherical and polyhedral particles that utilizes GPU for more efficient computation.

2.1 Contact model for spherical particles

The Hertz-Mindlin contact model is the most used model to describe the interaction between coarse non-cohesive particles and the surrounding geometry [12]. The normal force is fundamentally based on Hertzian contact theory [13], which determines a contact force using the contact overlap of two spheres. Decades later the model was improved by adding a tangential force-displacement relation for elastic spheres under frictional contact [14]. The normal force F_n is a function of the normal overlap δ_n, and is given by:

$$F_n = \frac{4}{3} E \sqrt{R} \delta_n^{3/2} \tag{1}$$

E is the equivalent Young's modulus, which is dependent on the Young's moduli of the two particles and the Poisson's ratio, and R is the equivalent radius of the two contacting spheres. The damping force F_n^d is subsequently described by:

$$F_n^d = -2\sqrt{\frac{5}{6}} \beta \sqrt{S_n m}\, v_n^{rel} \tag{2}$$

In this equation, $v_n^{rel}$is the relative velocity, S_n is the normal stiffness and β is a coefficient dependent on the coefficient of restitution. The tangential force, F_t, is dependent on the tangential overlap δ_t, the tangential stiffness S_t, and the tangential damping force F_t^d:

$$F_t = -S_t \delta_t \tag{3}$$

$$F_t^d = -2\sqrt{\frac{5}{6}}\beta\sqrt{S_t m}\, v_t^{rel} \tag{4}$$

A simplified scheme can be seen in **Figure 1,** and a more detailed model description is given in [15].

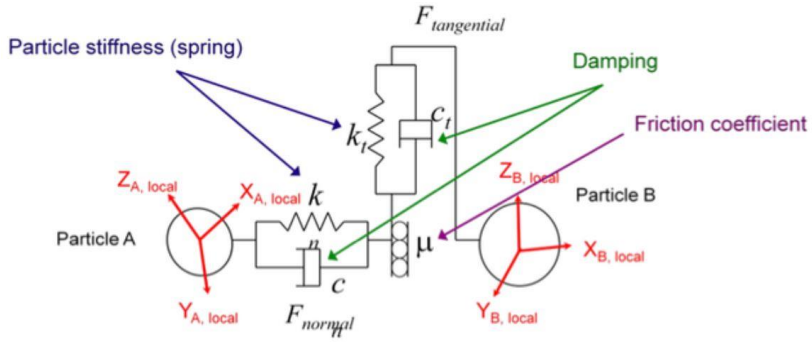

Figure 1: Schematic representation of a simplified Hertz-Mindlin contact model [15].

2.2 Contact model for polyhedral particles

For the implementation of polyhedral particles, the Nassauer-Kuna contact model is chosen [16]. In this contact model, each particle is approached as a volume inside a set of half-spaces. To calculate geometrical characteristics like volume, mass or moments of inertia, the faces have to be triangulated using their corner points. See **Figure 2a** and **2b** for a visual representation.

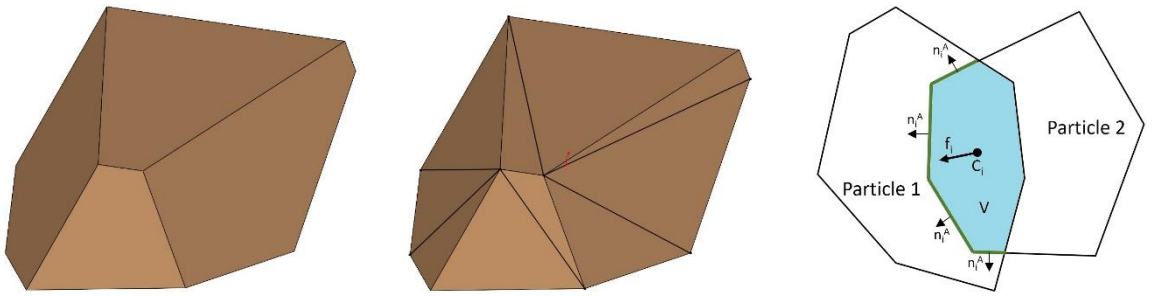

(a) 3D polyhedral particle

(b) Polyhedral particle with triangulation

(c) Contact detection of two particles

Figure 2: Polyhedral volume detection

For contact detection, the overlapping region is calculated as a set of half-spaces as well, which can be used for the calculation of interaction forces. In order to calculate the contact forces, the application point and the direction of the force have to be determined. The force application point is located at the center of mass C_i of the overlapping region, as illustrated in **Figure 2c**. To calculate the force direction n_i^f, the surface normal n_i^A of the overlapping region is integrated over the part of the surface that belongs to one of the particles. Additionally, the relative velocity v_i^{rel} of the particles at the force application point is considered, which consists

of both translational and rotational movements of the particles. The relative velocity is divided in a normal v_i^{reln} and tangential v_i^{reltn} component, and based on this the normal force f_i^n and tangential force f_i^n can be calculated [16]:

$$Normal\ Force\ =\ f_i^n = \underbrace{k^n V n_i^f}_{elastic\ force} - \underbrace{k^{nd} v_i^{reln}}_{viscous\ damping} \tag{5}$$

$$Tangential\ Force\ =\ f_i^t = \mu |f_i^n| \frac{v_i^{relt}}{|v_i^{\mathrm{relt}}|} \underbrace{\left(1 - \frac{0.1 + |v_i^{relt}|^2}{0.1}\right)}_{friction\ force} - \underbrace{k^{td} v_i^{relt}}_{viscous\ damping} \tag{6}$$

2.3 Particle shapes

To make a comparison of spherical, clumped spheres and polyhedral shape, five particle shapes are created which are visible in **Figure 3**. For the clumped spheres, two basic shapes are chosen. The spherical shape has a diameter of 30 mm, the other particle shapes are generated with the volume equivalent to the sphere.

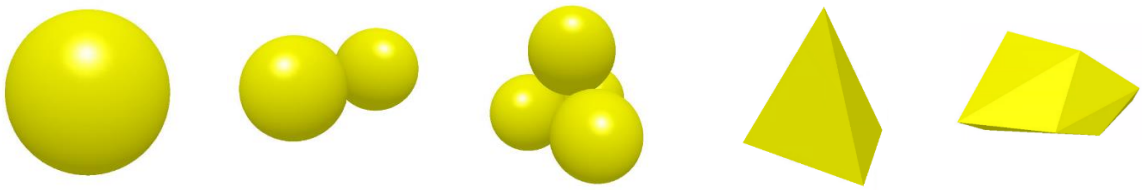

Figure 3: Modelled particle shapes, from left to right: sphere, two-sphere, four-sphere, tetrahedron, scanned.

The two implemented polyhedral shapes can be seen on the right of **Figure 3**. The tetrahedron is the simplest polyhedral, which is a similar geometrical representation to the "four-sphere". To investigate how realistic particle shapes perform, six scanned shapes of limestone particles with a size of 20-60 mm are used. The process of converting a real particle to a 3D file is shown in **Figure 4**. This particle shape has been created using a rotating table, and the 3D-scanning app QLone. For computational reasons, the number of vertices of one single scanned particle is reduced from the order of 10^4 to 20.

(a) Limestone particle **(b)** Particle scanning **(c)** 3D particle **(d)** Simplified shape representation

Figure 4: Particle scanning process of limestone particles

2.4 Key Performance Indicators (KPIs)

The measured KPIs are the penetration resistance, also called Work, and the porosity of the particle bed underneath the penetration tool. The Work is the integral of the total measured force on the geometry over penetration depth, which is expressed in Joules (J) (equation 7). The porosity, indicated by θ, is a dimensionless number which describes the packing of a material, and is derived from the bulk and particle density (equation 8). A low porosity indicates a more dense material bed.

$$W = \int_a^b F(x)\,dx \tag{7}$$

$$\theta = 1 - \frac{\rho_b}{\rho_p} * 100\% \tag{8}$$

3 SIMULATION SETUP

The following simulation has been created to investigate the packing and penetration resistance for several particle shapes. To minimize the boundary influences, the periodic boundary condition is applied in both x and y directions. Once a particle leaves the domain on one side, it automatically re-enters on the opposite side. Using this, a continuous particle bed can be simulated [15]. A particle bed with a height of approximately 0.7 m is created by randomly falling particles between 0 and 2.8 s (**Figure 5a**), after which the bed is consolidated with a certain pressure (**Figure 5b**). Finally, the penetration tool is inserted with a speed of 0.05 m/s, until a penetration depth of 0.3 m (**Figure 5c**).

Table 1: Simulation phases

Time	Phase
0 – 2.8 s	Generation of particle bed
2.8 – 4.2 s	Consolidation
5.0 – 17.5 s	Penetration

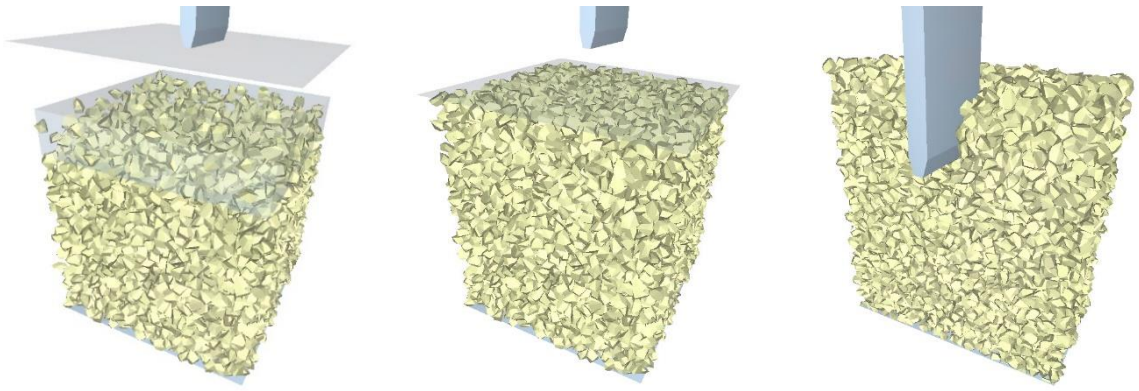

(a) Particle bed generation **(b)** Consolidation **(c)** Penetration

Figure 5: Visual representation of simulation phases for scanned particle shape

The constant input parameters of the simulations are given in **Table 2**, several properties like the particle density and sliding friction coefficient between particle and geometry have been determined experimentally in our previous study [3]. For the shear modulus and density of the geometry, standard input values have been chosen. The penetration plate has a height of 400 mm, a length of 200 mm and a thickness of 40 mm. At the tip of the penetration plate, the width decreases to a blunt tip of 20 mm (**Figure 6**).

Table 2: Constant input parameters

Property	Symbol	Unit	Value
Particle shear modulus	G_p	MPa	800
Rolling friction coefficient, p - p	$\mu_{r,p-p}$	-	0.5
Rolling friction coefficient, p - g	$\mu_{r,p-g}$	-	0.5
Sliding friction coefficient, p - g	$\mu_{s,p-g}$	-	0.642
Particle density	ρ_p	kg/m^3	2650
Particle diameter (median)	d_{50}	mm	30
Time step	Δt	s	1.32E-05
Poisson's Ratio	v	-	0.25
Geometry shear modulus	G_g	GPa	70
Geometry density	ρ_g	kg/m^3	7800

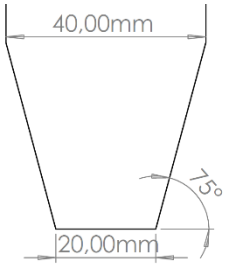

Figure 6: Plate tip geometry

For each particle shape, a base simulation is created of which the varying parameters are visible in the fourth column of **Table 3**. Subsequently, for each shape a sensitivity analysis is executed for the sliding friction, consolidation pressure and Particle Size Distribution (PSD). In the base simulation, only particles of the median diameter are included. In the first level of the PSD, a normal distribution with standard deviation $\sigma = 0.2 * d_{50}$ is implemented, and particle sizes are capped at 0.8 and 1.2 d_{50}. In the second level, the particles are equally distributed with 50% of the mass $0.8 * d_{50}$, and the other half of the particle sizes $1.2 * d_{50}$. No interaction of varying parameters is investigated, resulting in seven simulations per particle shape, including the base simulation. This leads to a total of thirty-five different simulations, which are repeated twice.

Table 3: Varying input parameters

Property	Symbol	Unit	Base	Level 1	Level 2
Sliding friction coefficient, p - p	$\mu_{s,p-p}$	-	0.5	0.3	0.7
Consolidation pressure	σ_{con}	kPa	150	0	300
Particle Size Distribution	PSD	-	Uniform	Norm, σ=0.2	0.8/1.2 *d_{50}

4 RESULTS

In this section, the results of previously described simulations are given and discussed. In the first section, the base simulations of the different particle shapes are compared quantitatively. Following this, a qualitative analysis of the impact of each varying parameter is addressed.

4.1 Base simulation results

The results of the force over penetration depth for each shape are presented in **Figure 7a.** The corresponding Work, the force integrated over depth was calculated by equation 7 and is presented in **Figure 7b.** The force versus depth curve shows a linear trend for all shapes. The fluctuations in force are not negligible, which are coming from the release and forming of contacts between geometry and particles. A difference in total resistance between particle shapes is noticeable, which could be due to the different implemented particle shapes. A remarkable observation is the low resistance of both polyhedral particle shapes compared to

the spherical and multi-spherical shapes. Even though the tetrahedron has a similar porosity as the four-spherical shape, the total resulting resistance (Work at maximum penetration depth) is by a factor of 1.9 lower.

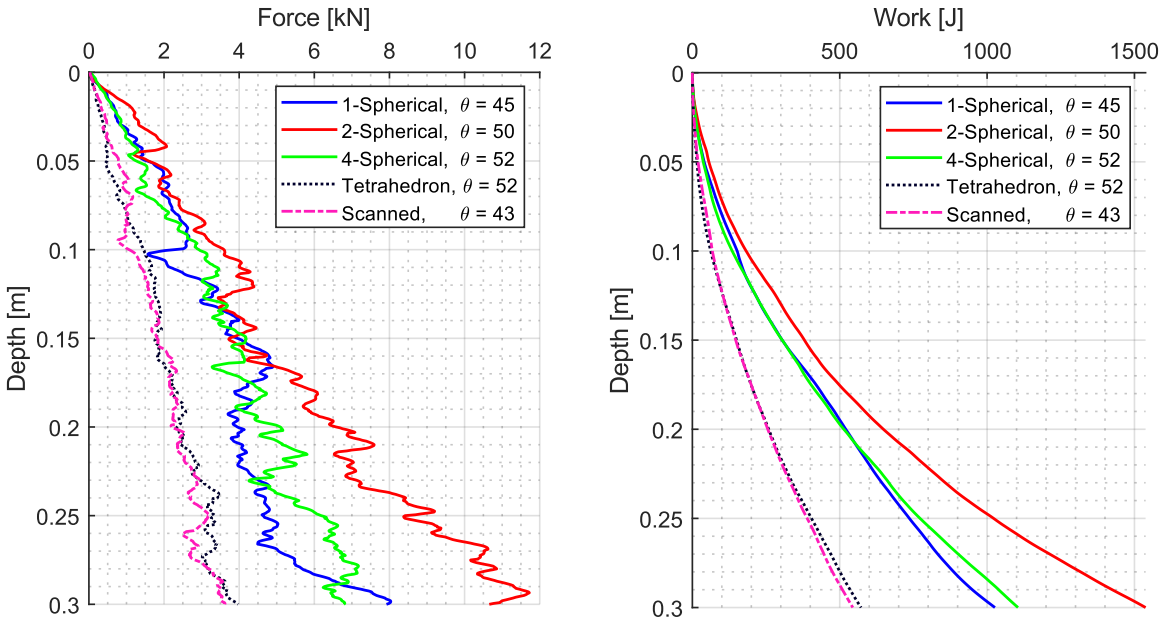

(a) Force vs penetration depth

(b) Work vs penetration depth

Figure 7: Resistance of penetration plate in particle bed for all shapes where θ denotes porosity achieved in the bed after consolidation.

The impact of consolidation pressure was measured by comparing the porosity before and after consolidation. The impact of consolidation pressure on the porosity is very small, with an average decrease of 0.93% in porosity for the spherical and multi-spherical shapes, and an average decrease of 1.51% in porosity for both polyhedral shapes. The small reduction in porosity for all particle shapes is as expected as this is a fully elastic contact model. When investigating position plots of the positions of the particles before and after consolidation, it was found that the rearrangement of particles is negligible.

4.2 Impact of varying parameters

The effect of the three varying parameters: interparticle sliding friction, consolidation pressure and PSD (levels are presented in **Table 3**), are determined by calculating the average impact on resistance (W_{avi}) and porosity (θ_{avi}) and comparing these to the base simulation by equations 9 and 10.

$$W_{avi} = \frac{|W_n - W_{base}|}{W_{base}} * 100\% \tag{9}$$

$$\theta_{avi} = \frac{|\theta_n - \theta_{base}|}{\theta_{base}} * 100\% \tag{10}$$

For each level of the varying parameter, two repetitions have been run, and the average absolute difference from the base simulation of all three simulations has been plotted.

For every particle shape, lowering the static friction decreases the resistance, whereas an increase in static friction has the opposite effect. The same holds for the consolidation pressure, a lower consolidation pressure results in a lower resistance, and applying a higher pressure raises the resistance. For both the different PSDs, the resistance is increased. From **Figure 8** it is clearly visible that changing the sliding friction coefficient has the most impact on the resistance of the particle bed, with reducing the sliding friction having more effect than increasing the sliding friction. This could be due to the fact that the relative decrease in sliding friction from 0.5 to 0.3, is bigger than the increase for the 2nd level.

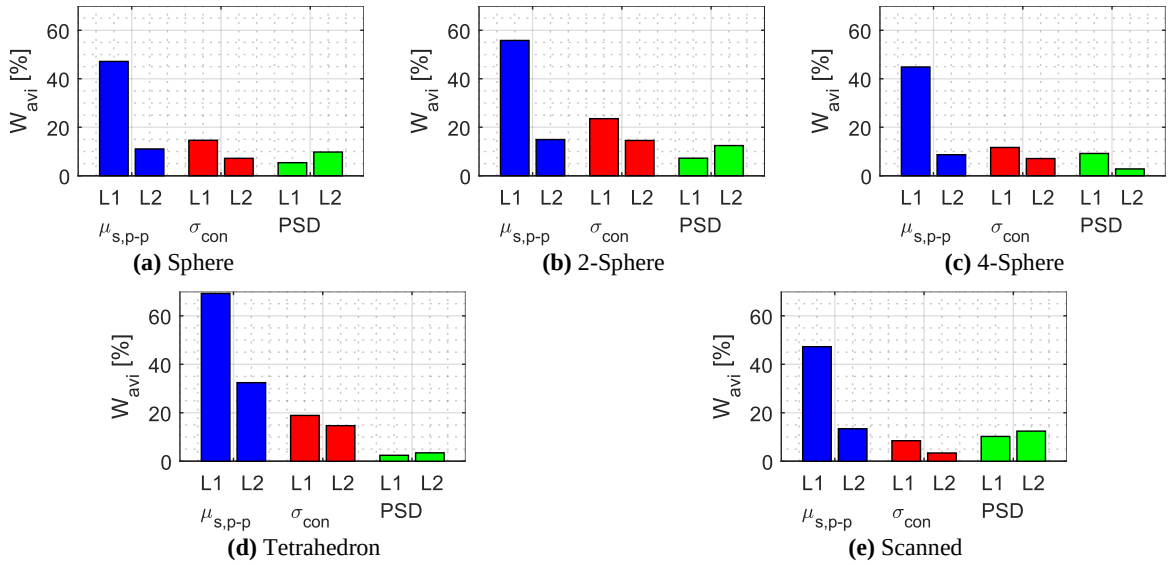

Figure 8: Average impact on resistance (W_{avi}) of varying parameters on base simulation

Figure 9 shows the average impact of each varying parameter on the porosity. A decrease in static friction leads to a decrease in porosity, whereas a decrease in consolidation pressure has the reverse effect. For both levels of the PSD, the porosity is further decreased. Of all three parameters, the consolidation pressure has the least impact for all particle shapes. It does however have a significant effect on the resistance of the particle bed, which could be due to rearrangement of the particles on the top layer of the particle bed. The initial penetration resistance will be higher, which could have an increasing effect on the overall penetration resistance. For all the shapes, level 2 of the PSD has a bigger decrease in porosity compared to level 1, which should result in a higher resistance, as the particle bed is more dense. An exception is visible for the 4-spherical shape, where level 1 has a higher resistance. This could be attributable to the general relatively small change in porosity (~1.5%), which is in the range of deviations, subsequently no clear explanation can be given for this behaviour.

An additional remarkable observation is that the relative change to the base simulation in resistance is in most cases higher than in the case of porosity. For example, level 1 of the PSD of the tetrahedron has a decrease in porosity of 2.2%, which leads to an increase in resistance of 18.9%.

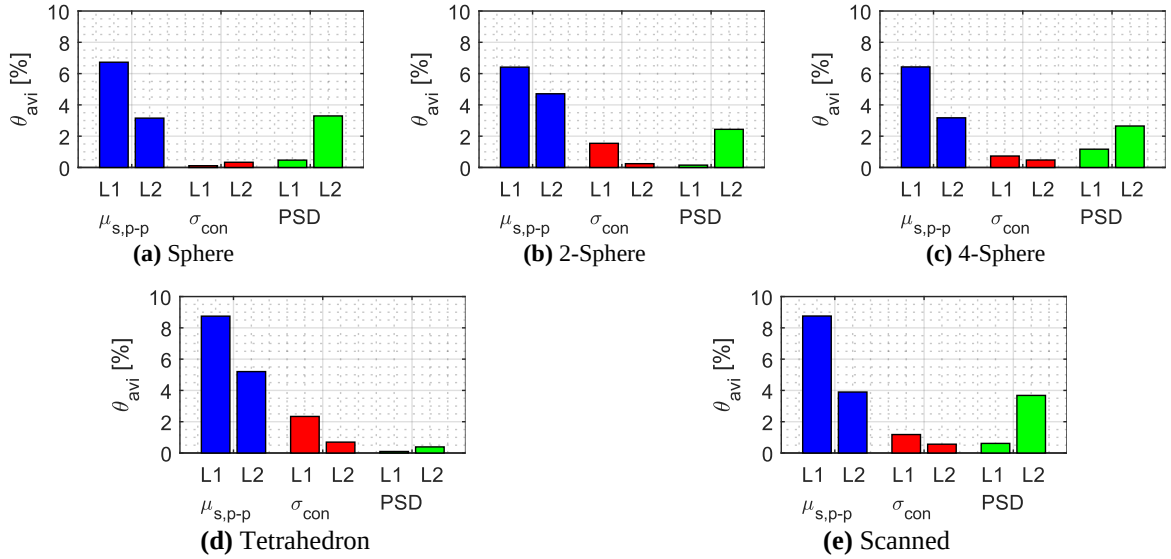

Figure 9: Average impact on porosity (θ_{avi}) of varying parameters on base simulation

5 CONCLUSIONS

The influence of particle shape on the penetration resistance is investigated by a plate penetration test in DEM. The penetration resistance is significantly impacted by the particle shape, however this is not correlated to the impact that particle shape has on the porosity. Especially using multi-spherical particle shapes, a higher porosity does not have to result in a lower resistance.

In general, polyhedral shapes exhibit lower penetration resistance compared to spherical and multi-spherical shapes. This could be due to the implementation of the rolling friction, which is different for spherical and polyhedral contact models. To fully understand the underlying mechanisms responsible for this behaviour, a further in-depth investigation is recommended.

Compression of the particle bed has minimal impact on the porosity due to the elastic non-cohesive behaviour of granular material. To gain a more comprehensive understanding, future research could explore the impact of keeping the particle bed in a loaded consolidated state.

Sliding friction between particles has been identified as the most influential factor on both resistance and porosity for all the particle shapes. In general, a small change in porosity can lead to a more pronounced change in resistance, highlighting the sensitivity of this parameter.

Overall, this study provides valuable insights into the role of particle shape in granular material modelling and lays the foundation for further advancements in the field.

REFERENCES

[1] J. Chen, R. Gao, and Y. Liu, 'Numerical Study of Particle Morphology Effect on the Angle of Repose for Coarse Assemblies Using DEM', *Advances in Materials Science and Engineering*, vol. 2019, p. e8095267, Sep. 2019, doi: 10.1155/2019/8095267.

[2] A. Khosravi, A. Martinez, and J. Dejong, 'DEM simulations of CPT measurements and soil classification', *Canadian Geotechnical Journal*, vol. 57, Nov. 2019, doi: 10.1139/cgj-2019-0512.

[3] G. J. Selm, van, 'Design of grabs for coarse material: Enhancing the penetration and cutting depth for limestone'. Delft University of Technology, Jan. 23, 2023. [Online]. Available: http://resolver.tudelft.nl/uuid:9a14f22a-7d85-4ab5-b1b6-1ebf57bd2f72

[4] S. W. Lommen, D. L. Schott, M. Rahman, and G. Lodewijks, 'The penetration of iron ore pellets: Calibrating discrete element parameters using penetration tests', *Proceedings of the 11th Particulate System Analysis Conference*, p. 5, 2011.

[5] N. Duan, Y. P. Cheng, and J. W. Liu, 'DEM analysis of pile installation effect: comparing a bored and a driven pile', *Granular Matter*, vol. 20, no. 3, pp. 1–16, 2018, doi: 10.1007/s10035-018-0805-2.

[6] N. Zhang, M. Arroyo, M. O. Ciantia, A. Gens, and J. Butlanska, 'Standard penetration testing in a virtual calibration chamber', *Computers and Geotechnics*, vol. 111, pp. 277–289, Jul. 2019, doi: 10.1016/j.compgeo.2019.03.021.

[7] B. Cerfontaine, M. J. Brown, M. Ciantia, M. Huisman, and M. Ottolini, 'Discrete Element Modelling of Silent Piling Group Installation for Offshore Wind Turbine Foundations', in *Proceedings of the Second International Conference on Press-in Engineering 2021, Kochi, Japan*, CRC Press, 2021.

[8] S. W. Lommen, M. Mohajeri, G. Lodewijks, and D. L. Schott, 'DEM particle upscaling for large-scale bulk handling equipment and material interaction', *Powder Technology*, vol. 352, 2019, doi: 10.1016/j.powtec.2019.04.034.

[9] C. J. Coetzee, 'Calibration of the discrete element method and the effect of particle shape', *Powder Technology*, vol. 297, pp. 50–70, Sep. 2016, doi: 10.1016/j.powtec.2016.04.003.

[10] S. Ji and L. Liu, 'Constructions of Irregular Shaped Particles in the DEM', in *Computational Granular Mechanics and Its Engineering Applications*, S. Ji and L. Liu, Eds., in Springer Tracts in Mechanical Engineering. Singapore: Springer, 2020, pp. 23–49. doi: 10.1007/978-981-15-3304-4_2.

[11] Z. Bibak and S. Banisi, 'A combined physical and DEM modelling approach to investigate particle shape effects on load movement in tumbling mills', *Advanced Powder Technology*, vol. 32, no. 3, pp. 916–930, Mar. 2021, doi: 10.1016/j.apt.2021.01.034.

[12] R. Qin *et al.*, 'Study on Physical and Contact Parameters of Limestone by DEM', *IOP Conf. Ser.: Earth Environ. Sci.*, vol. 252, p. 052110, Jul. 2019, doi: 10.1088/1755-1315/252/5/052110.

[13] Hertz, H., 'On the contact of elastic solids.', *Journal für die reine und angewandte Mathematik*, vol. 91, pp. 156–171, 1882.

[14] R. D. Mindlin and H. Deresiewicz, 'Elastic spheres in contact under varying oblique forces', *J. App. Mech.*, vol. 75, pp. 327–344, 1953.

[15] Altair, 'EDEM 2022.3 User Guide'. 2023.

[16] B. Nassauer, T. Liedke, and M. Kuna, 'Polyhedral particles for the discrete element method', *Granular Matter*, vol. 15, no. 1, pp. 85–93, Feb. 2013, doi: 10.1007/s10035-012-0381-9.